Full length article

In-situ SEM observation of phase transformation and twinning mechanisms in an interstitial high-entropy alloy

Meimei Wang[*], Zhiming Li, Dierk Raabe

Max-Planck-Institut für Eisenforschung, Max-Planck-Straße 1, 40237 Düsseldorf, Germany

ARTICLE INFO

ABSTRACT

The recently developed interstitial high-entropy alloys (iHEAs) exhibit an enhanced combination of strength and ductility. These properties are attributed to dislocation hardening, deformation-driven athermal phase transformation from the face-centered cubic (FCC) γ matrix into the hexagonal close-packed (HCP) ε phase, stacking fault formation, mechanical twinning and precipitation hardening. For gaining a better understanding of these mechanisms as well as their interactions direct observation of the deformation process is required. For this purpose, an iHEA with nominal composition of Fe-30Mn-10Co-10Cr-0.5C (at. %) was produced and investigated via *in-situ* and interrupted *in-situ* tensile testing in a scanning electron microscope (SEM) combining electron channeling contrast imaging (ECCI) and electron backscatter diffraction (EBSD) techniques. The results reveal that the iHEA is deformed by formation and multiplication of stacking faults along {111} microbands. Sufficient overlap of stacking faults within microbands leads to intrinsic nucleation of HCP ε phase and incoherent annealing twin boundaries act as preferential extrinsic nucleation sites for HCP ε formation. With further straining HCP ε nuclei grow into the adjacent deformed FCC γ matrix. γ regions with smaller grain size have higher mechanical stability against phase transformation. Twinning in FCC γ grains with a size of ~10 μm can be activated at room temperature at a stress below ~736 MPa. With increasing deformation, new twin lamellae continuously nucleate. The twin lamellae grow in preferred directions driven by the motion of the mobile partial dislocations. Owing to the individual grain size dependence of the activation of the dislocation-mediated plasticity, of the athermal phase transformation and of mechanical twinning at the different deformation stages, desired strain hardening profiles can be tuned and adjusted over the entire deformation regime by adequate microstructure design, providing excellent combinations of strength and ductility.

© 2018 Acta Materialia Inc. Published by Elsevier Ltd. All rights reserved.

1. Introduction

High-entropy alloys (HEAs) attract high attention as they tap a sheer infinite elemental composition space, offering opportunities for discovering novel properties and their combinations [1—15]. The recently developed interstitial high-entropy alloys (iHEAs) open this pathway even further owing to the huge leverage that small elements on inter-lattice sites render on constitution and properties, as is also known from many steels. More specific, some iHEAs exhibit enhanced combinations of strength and ductility, due to activation of practically all possible strengthening effects, e.g. interstitial and substitutional solid solution strengthening,

twinning-induced plasticity (TWIP), transformation-induced plasticity (TRIP), composite effects, precipitation hardening, work hardening by dislocations and stacking faults as well as grain refinements [12,16]. The mixing entropy pertaining to the Fe-30Mn-10Co-10Cr-0.5C (at. %) iHEA (studied in this work) is relatively low compared to those HEAs with more than 5 principal elements in equimolar fraction [1,4,16,17]. The authors noted that the maximized configurational entropy is not the sole factor determining phase stability of HEAs. Indeed, previous work of the current authors on the development of novel TRIP-assisted dual-phase HEAs has been motivated by the facts that first, both enthalpy and entropy together determine alloy stability and second, the absence of detrimental intermetallics is in some cases a more essential boundary condition for successful alloy design than entropy maximization alone [4,17]. Our main point is thus more placed on arriving at a stacking-fault energy dependent point of phase

---

* Corresponding author.
  E-mail address: m.wang@mpie.de (M. Wang).

metastability for obtaining more superior mechanical properties through the associated athermal deformation driven transformation mechanisms.

Among these aforementioned deformation mechanisms, mechanical twinning is the most extensively studied effect [8—15]. The activation of mechanical twinning has been reported to effectively enhance strain hardening of HEAs at cryogenic, i.e. liquid nitrogen temperature [11,13]. The characterization techniques mainly employed so far in that context included electron backscatter diffraction (EBSD), transmission electron microscopy (TEM) and neutron-diffraction based techniques. EBSD allows mapping of the evolution of crystallographic features as a result of mechanical twinning, e.g. local and global grain orientations, kernel average misorientations and geometrically necessary dislocations (GNDs) at a wide field of view [12,13,15]. By employing TEM, the formation of stacking faults (SFs), nucleation and growth of twinning are revealed [8,10]. By employing *in-situ* neutron diffraction, the evolution of mechanical twinning was evaluated based on the evolution of the stacking fault probability [9].

In contrast to mechanical twinning, phase transformation in HEAs is less commonly studied [5—7]. Synchrotron X-ray diffraction (SXRD) and TEM have been employed to characterize phase transformation products in HEAs. While the influence of grain orientation on deformation-driven phase transformation can be studied by SXRD [5] and the transformation products can be revealed by dark-field diffraction in TEM [6,7], the transformation kinetics associated with these phenomena are still unknown. In addition, deformation-driven phase transformations are rapid and diffusionless. This means that in HEAs more detailed *in-situ* tracking of the nucleation and growth of deformation-driven phase transformation products during deformation is a pending challenge.

Yet, for designing HEAs and iHEAs with enhanced mechanical properties, detailed understanding of all active deformation mechanisms and their interaction is essential. Particularly the magnitude of the stacking fault energy (SFE), which is mainly controlled by chemical composition and temperature, is an important factor controlling activation of these multiple coexisting and competing deformation mechanisms [18—22]. For avoiding possible effects of compositional inhomogeneity on the SFE and the associated deformation mechanisms in different samples, it is therefore preferable to sequentially map microstructure evolution in the same region, i.e. via *in-situ* testing. Since microstructure evolution is then monitored in the same material portion, *in-situ* straining also allows to better reveal direct links among dislocation and partial dislocation activities, mechanical twinning and phase transformation. However, such insights, when obtained from deformation of thin foil specimens exposed to *in-situ* TEM probing, are sometimes not fully transferable to bulk materials owing to foil and surface related mechanical boundary condition effects. Also, TEM reveals microstructure features in a relatively confined region. Similar arguments hold for *in-situ* SXRD/neutron diffraction methods due to low direct spatial microstructure correlation. Some of these shortcomings can be overcome by probing microstructure, dislocations and crystallographic texture using *in-situ* high resolution scanning electron microscopy (SEM) [23—26]. By using bulk samples, *in-situ* high resolution SEM is capable of unraveling deformation mechanisms in bulk materials. Due to its large field-of-view and high spatial resolution (down to ~80 nm) [27], interrupted *in-situ/in-situ* EBSD based on high-resolution SEM has proven itself as a powerful tool to study phase transformations in many systems, e.g. multi-phase TRIP steels [25,26,28], quench and partitioning steels [29,30], and high-Mn austenitic steels [31,32]. As a SEM-based tool with high spatial resolution, e.g. ~2.9 nm using an acceleration voltage of 30 kV and a beam current of 11.6 nA,

electron channeling contrast imaging (ECCI) has been successfully applied to the observation of dislocations, partial dislocations and mechanical twinning in many systems [28,33—37]. Here we therefore use the combination of *in-situ* and interrupted *in-situ* joint EBSD and ECCI probing in the SEM as a wide field of view method for directly observing activation of dislocations, stacking faults (SFs), mechanical twinning and displacive phase transformation with the aim to unravel the strain hardening mechanisms in a iHEA.

2. Experimental procedures

The nominal chemical composition of the iHEA is Fe-30Mn-10Co-10Cr-0.5C (at. %). The alloy was cast in a vacuum induction furnace, hot rolled and homogenized at 1200 °C for 2 h, followed by water quenching. The alloy was cold rolled to ~60% total thickness reduction in several rolling passes and then annealed at 900 °C for 3 min under Ar atmosphere, and eventually quenched in water.

To reveal the elemental distribution and characterize the microstructure, energy-dispersive X-ray spectroscopy (EDX), EBSD and ECCI probing in the SEM were employed. Samples were prepared by grinding, polishing in diamond suspension and final polishing in colloidal silica suspension for ~1.5 h. The last step ensures that the sample surface is deformation-free. EDX mapping was conducted in Zeiss-Merlin at 15 kV. EBSD measurements were carried out at 15 kV with a step size of 80 nm using a JEOL JSM-6500F instrument. For ECCI measurements, a Zeiss-Crossbeam XB 1540 FIB-SEM and a Zeiss-Merlin instrument were used each operated at an acceleration voltage of 30 kV.

To track the phase transformation and correlate it with the deformation substructure, interrupted *in-situ* EBSD and ECCI observations of the same sample regions were conducted, consisting in the repeated observation of the same material portions during interrupted tensile testing at different strain levels. Deformation was imposed as a uniaxial tensile load on dog-bone samples at room temperature with an initial strain rate of 10^{-3}/s using a Kammrath and Weiss tensile stage. After deforming the sample to pre-defined strain levels, it was unmounted and transferred to SEM for microstructure characterization.

To additionally track the evolution of microstructure during deformation without interrupting loading, *in-situ* tensile testing was conducted using a Zeiss-FIB SEM with a home-built tensile stage. Prior to the *in-situ* tensile test, EBSD measurements were carried out on polished sample in the undeformed state. Then ECC images of same regions were taken both in the undeformed state and after different strain levels without unloading the sample. All strain values obtained both, during the interrupted *in-situ* and the *in-situ* tests were calculated by measuring the local length changes of the investigated regions along the loading direction.

3. Results

3.1. Microstructure in the undeformed state and mechanical properties

The microstructure and elemental distribution in the undeformed state are shown in Fig. 1. SEM EDX mapping reveals homogeneous distribution of all elements at the grain scale (Fig. 1b—e). Thus, a specific influence of compositional inhomogeneity on the phase transformation and twinning kinetics can be excluded. The true stress-strain and strain hardening curves are shown in Fig. 1f. Since true strain is calculated from engineering strain following the constraint of constant volume, no true strain can be calculated anymore after necking, thus the data is presented up to the end of uniform deformation (prior to necking). The iHEA
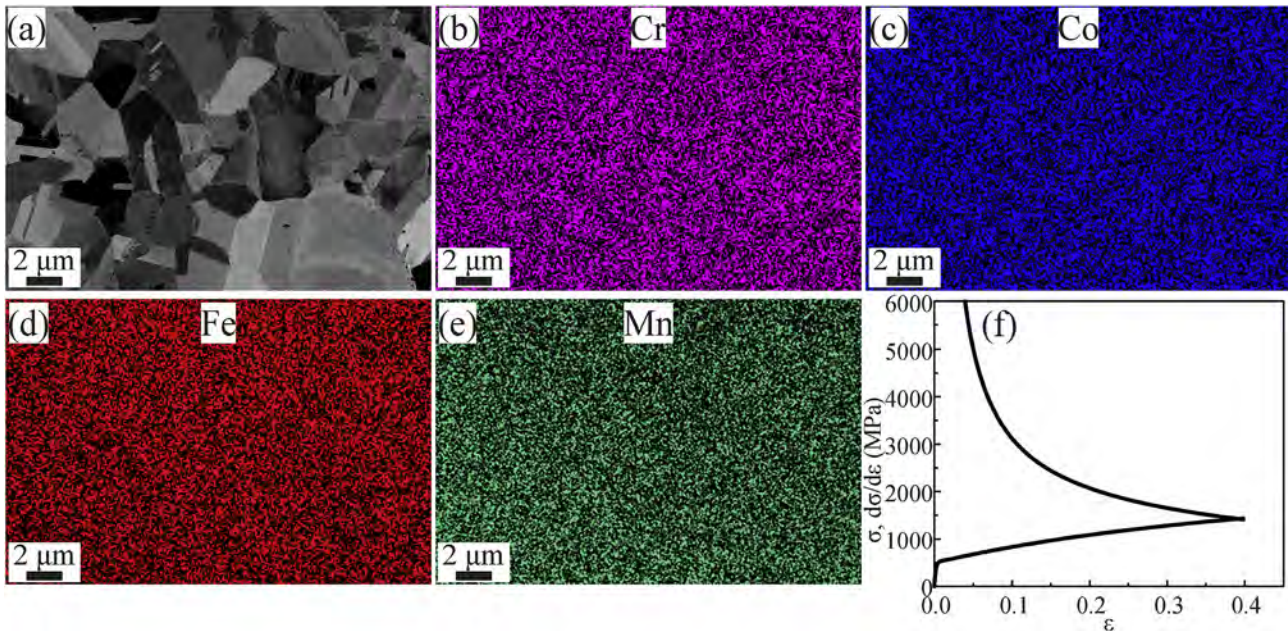
Fig. 1. Microstructure and elemental distribution in the iHEA in undeformed state. (a) Backscatter electron image of the microstructure. Distribution of (b) Cr; (c) Co; (d) Fe; (e) Mn, measured by SEM EDX. (f) True stress and strain hardening with respect to true strain.

shows a yield strength of ~500 MPa, ultimate tensile strength of ~960 MPa, uniform elongation of ~53% and total elongation of ~61%. Note that except the true stress strain curve presented in Fig. 1f, all strain values used in this work are referred to as engineering strains.

3.2. Interrupted in-situ EBSD observation of deformation-induced phase transformation

Fig. 2 shows the microstructure evolution with increase in local strain from 0% to 20% during interrupted *in-situ* EBSD measurements. The grain size map of the alloy in undeformed state is shown in Fig. 2a using a rainbow color code, e.g. grains in red are larger than grains in blue. In the undeformed state, the microstructure

consists of FCC γ phase and small amounts of thermally-induced HCP ε phase (~0.2% area fraction) (Fig. 2b). After straining to 10%, formation of deformation-induced HCP ε phase can be observed in ~0.5% area fraction of the grains (Fig. 2c). With further straining to 14%, and then to 20%, a gradual increase in the deformation-induced HCP ε phase fraction occurs to an area fraction of ~1.2% and then to ~2.0%, respectively (Fig. 2d and e). Two factors influence these findings, namely, the increasing surface roughness and the associated resolution limits of EBSD. More specific, the increasing deformation and surface roughness reduce the resolution of the EBSD measurement. When low EBSD confidence index regions (<0.1) are filtered out, the non-indexed area fraction increases form ~1.2% area fraction in the undeformed state to ~31.6% area fraction at 20% strain (black points in the EBSD maps). Regarding the second
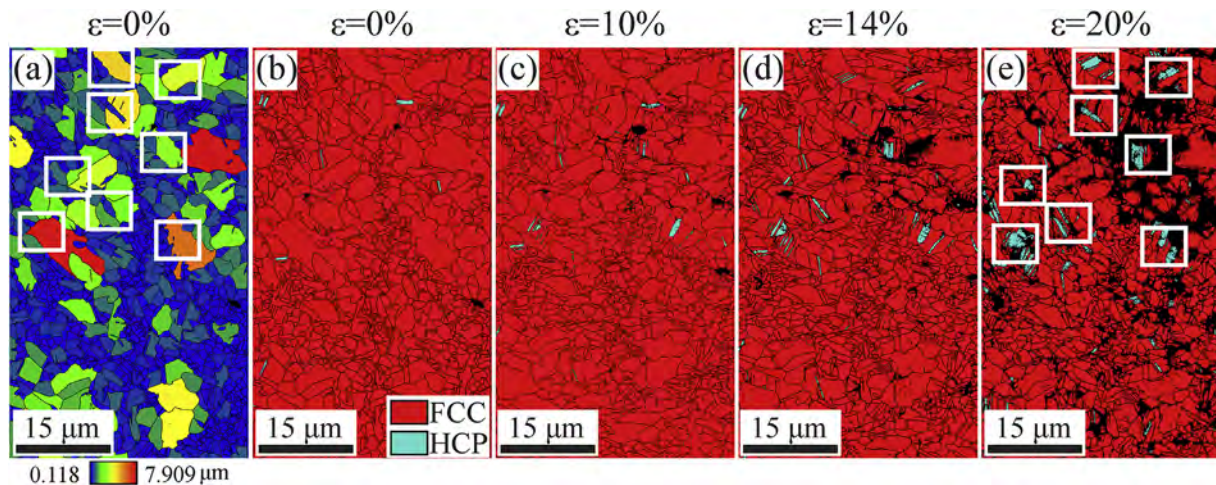

Fig. 2. Interrupted *in-situ* observation of deformation-driven phase transformation during tensile loading. (a) EBSD grain size map in the undeformed state; (b–e) phase map at global tensile where red represents FCC γ and blue represents HCP ε. High angle boundaries with misorientations >15° are overlaid on all maps as black lines. Some grains are highlighted by white color rectangles in the grain size map and phase map to reveal the grain size dependence of the transformation kinetics. (For interpretation of the references to color in this figure legend, the reader is referred to the Web version of this article.)

aspect, at an EBSD step size of 80 nm and a standard of at least two pixels per grain HCP ε grains below 160 nm are not reliably captured. Thus, the increase in area fraction of deformation-induced ε phase amounts to 1.8% between the undeformed state and 20% strain, while the experimental limitations explained above give a scatter a bar of about 30%.

Few locations where deformation-induced HCP ε phase is formed at 20% strain are highlighted by white rectangles in Fig. 2e. When tracking grain size map in undeformed state, it is obvious that these FCC γ host grains with high tendency towards HCP ε formation assume larger grain size, i.e. lower mechanical stability against deformation-induced athermal phase transformation (Fig. 2a and b).

For analyzing the progress in deformation and phase transformation in more detail, one region from Fig. 2 has been exemplarily cropped and magnified in Fig. 3. In the undeformed state, the microstructure in this area consists of FCC γ grains and two thermally-induced HCP ε martensite plates, as highlighted by the white arrows (Fig. 3a$_1$). The defect density inside the γ grains is revealed in terms of the kernel average misorientation (KAM) map in Fig. 3c. The KAM value is a measure of the average misorientation of the neighboring orientation points relative to a given center orientation point. Here the 2nd neighbor shell has been considered. Misorientations >5° are discarded to avoid an artificial influence from adjacent grain boundaries. Thus, the KAM measure is here used as an index for representing the accumulated local lattice curvature due to plastic deformation [38—40]. In the undeformed state, only low angle grain boundaries are associated with high KAM values (Fig. 3c$_1$). At 10% strain, a parallel pattern consisting of deformation-induced HCP ε lamellae has been formed within the FCC γ grains, as highlighted in terms of the yellow arrows (Fig. 3a$_2$). These deformation-induced HCP ε lamellae formed in the same FCC γ host grain carry the same crystallographic orientation (Fig. 3b$_2$). The remaining part of the FCC γ grain also exhibits an increase in the KAM values, indicating simultaneous deformation of the FCC γ

host grain and the simultaneous occurrence of deformation-driven phase transformation (Fig. 3c$_2$). With increasing straining to 14% and 20%, formation of new deformation-induced HCP ε lamellae is observed (Fig. 3a$_3$, a$_4$). Furthermore, the previously formed deformation-induced HCP ε lamellae thicken and grow towards each other, leading finally to the formation of large blocks of deformation-induced HCP ε phase regions (Fig. 3a$_3$, a$_4$). All deformation-induced HCP ε phase formed within the same FCC γ grains maintain the same crystallographic orientation (Fig. 3b$_2$-b$_4$). The remaining segments of FCC γ grains gradually rotate away from their original orientation with increasing deformation, indicating further strain accommodation inside the remaining γ grains (Fig. 3b$_2$-b$_4$). This is also consistent with the increased KAM values in these γ grains with further straining (Fig. 3c$_2$-c$_4$).

3.3. In-situ ECCI observation of deformation structure evolution

For revealing deformation features inside the FCC γ grains we conducted in-situ testing in conjunction with ECCI mapping in the SEM, Fig. 4. The engineering stress strain curves monitored during the in-situ test are given above the substructure images where blue circles indicate the corresponding strains. Fig. 4a and b shows examples of large (grain size ~7.8 μm) and small (grain size ~3 μm) FCC γ grains, respectively. When increasing the local strain to 6.7%, both grains develop SFs, which are the features with white contrast in the ECC images (Fig. 4a$_2$, b$_2$). In ECC images, SFs are characterized by white contrast features bounded by a straight bright line on one side and fading contrast on the opposite side [33]. The orientation of these SFs, as indicated by black lines, are parallel with {111} slip traces indicated by red lines (Fig. 4a$_2$, b$_2$). When strained to 10.1% and further to 12.4%, a higher density of SFs and a corresponding reduction in their mean spacing are observed (Fig. 4a$_3$ to a$_4$, Fig. 4b$_3$ to b$_4$). These {111} crystallographically oriented strain localization bands with accumulations of dislocations and SFs are microbands [17,41]. Comparing the deformation patterns in the big and small γ
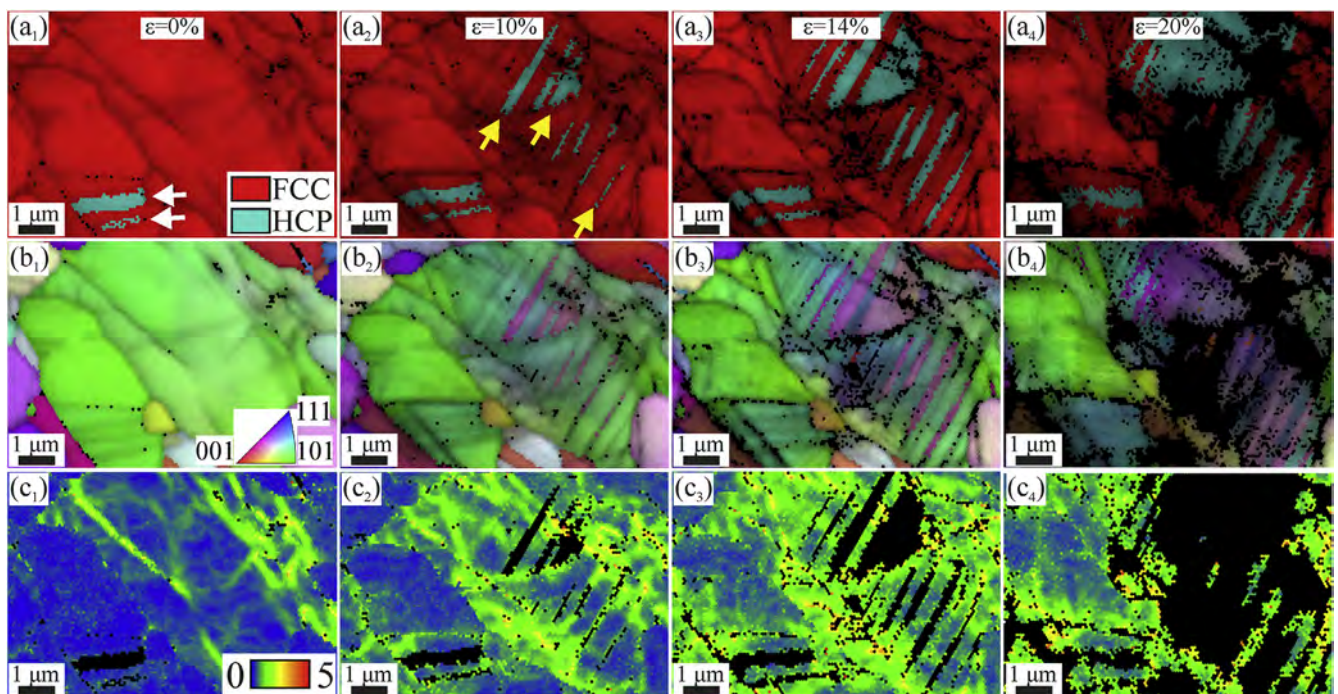

Fig. 3. Microstructure evolution revealed exemplarily on a cropped region taken during interrupted in-situ EBSD tensile testing, characterized in terms of (a) phase map; (b) IPF map; and (c) KAM map of FCC γ grains at local strain of (1) ε = 0%; (2) ε = 10%; (3) ε = 14%; and (4) ε = 20%. In the phase maps, red represents FCC γ and blue represents HCP ε. IPF: inverse pole figure; KAM: Kernel average misorientation. (For interpretation of the references to color in this figure legend, the reader is referred to the Web version of this article.)
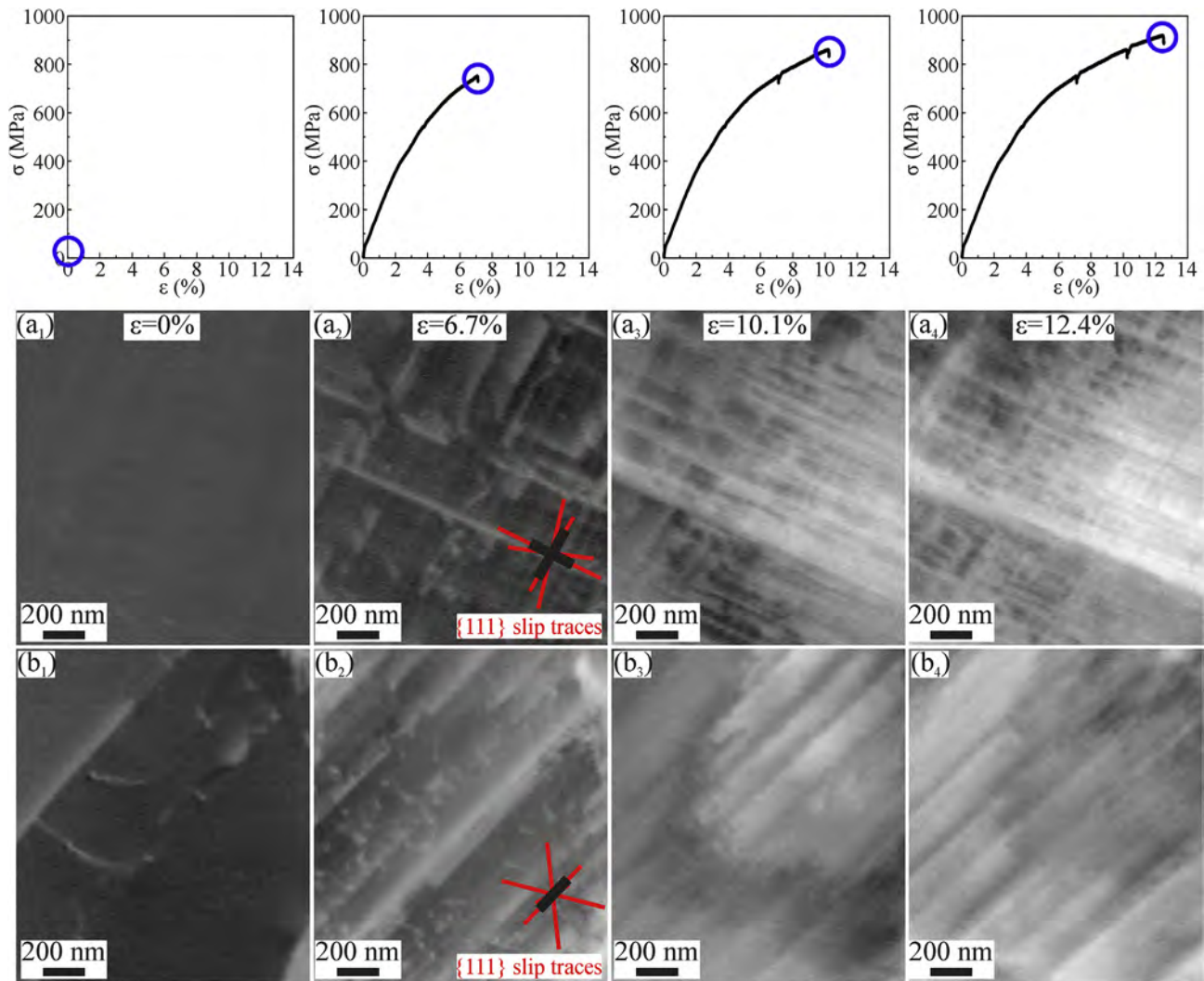
Fig. 4. *In-situ* ECCI observations of SF formation during tensile testing in (a) large (grain size ~7.8 μm); and (b) small (grain size ~3 μm) FCC γ grains. The engineering stress strain curves given above indicate the corresponding strains.

grains after 12.4% strain reveals that the density of microbands is much higher in the former than in the latter (Fig. 4a$_4$, b$_4$).

3.4. Interrupted in-situ EBSD and ECCI observations of coupling between plastic deformation and phase transformation

Fig. 5 presents results obtained from the direct coupling of deformation and phase transformation from FCC γ to HCP ε observed by interrupted *in-situ* testing. Two regions with different crystallographic orientations are shown as examples. For each area, the EBSD phase map and the associated ECC images are presented for different strain levels. For area 1, in the undeformed state, the annealing twin boundary map is overlaid on the phase map as yellow lines (Fig. 5a$_1$). Similar as in Fig. 4, with increasing deformation to 10%, an increase in the density of SFs is observed (Fig. 5b$_1$, b$_2$). They form along {111} planes (black lines) and are accompanied by {111} slip traces (red lines). At 14% strain the density of SFs increases (Fig. 5b$_3$) and formation of HCP ε in the deformed structure is observed (Fig. 5a$_3$). Increasing the strain to 20% reduces the spacing among the microbands. These are also preferred regions where deformation-induced HCP ε forms until it has fully transformed the microbands (Fig. 5a$_4$). This consecutive and associated

deformation and phase transformation behavior is also observed in region 2 (Fig. 5c and d). When analyzing the character of the grain boundaries associated with the nucleation of HCP ε in the two regions, we find that annealing twin boundaries (yellow lines) act as preferential nucleation sites (Fig. 5a$_1$, c$_1$).

3.5. In-situ ECCI observation of mechanical twinning

Besides the deformation-driven phase transformation, mechanical twinning can also be directly observed *in-situ* via ECCI probing such as shown in Fig. 6. An overview of the microstructure evolution during deformation is presented in Fig. 6a, where drastic changes in contrast due to the evolving surface roughness and crystal rotation can be observed. Two lamellae of annealing twins are present in this grain (grain size ~10 μm) in the undeformed state (Fig. 6b$_1$). After a local sample strain of 6.7%, nucleation of mechanical twinning occurs, as indicated by yellow arrows (Fig. 6b$_2$). Mechanical twining can be distinguished from SFs in the SEM due to the sharp contrast with respect to the hosting FCC γ grains on both sides of the twin [16]. The corresponding global engineering stress at a local engineering strain of 6.7% is ~736 MPa. Also the dislocation density in the FCC γ grains increases with ongoing
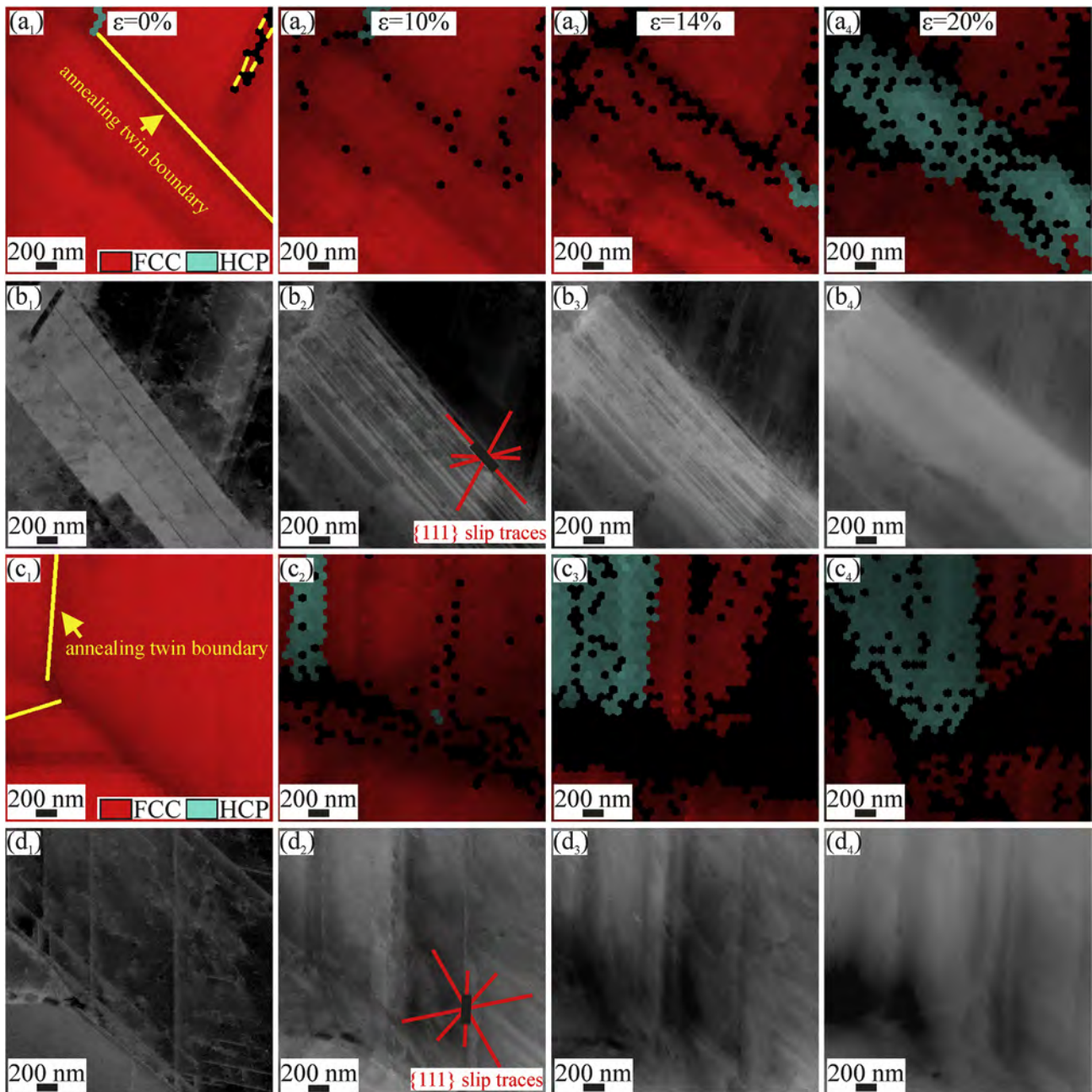
Fig. 5. Interrupted *in-situ* EBSD and ECCI observations of deformation and phase transformation in the iHEA. (a) Overlay of phase map with image quality map; and (b) ECC image of region 1. (c) Overlay of phase map with image quality map; and (d) ECC image of region 2. In Fig. 5b$_2$ and d$_2$, {111} slip traces are indicated by red lines and alignment of microbands is indicated by black line. In the phase map (undeformed state) the annealing twin boundaries are plotted as yellow lines. (For interpretation of the references to color in this figure legend, the reader is referred to the Web version of this article.)

deformation. With further straining to 10.1% and then to 12.4%, thickening and further nucleation of twins is observed (Fig. 6b$_3$, b$_4$). The thickening of the twin lamellae proceeds primarily in one direction.

3.6. Evolution of crystallographic texture during interrupted in-situ EBSD deformation

The evolution of the crystallographic texture of both, the FCC γ and the HCP ε phases as observed during an interrupted *in-situ* tensile testing is shown in Fig. 7 for a local engineering strain up to 20%. For the γ phase, a {111}//TA (tensile axis) deformation texture

is gradually built up. In the undeformed state, only a few thermally-induced ε lamellae are present in the microstructure (Fig. 2b), forming a preferred texture component with high orientation density (Fig. 7b$_1$). With the further continuous nucleation and growth of deformation-induced ε, a new {10−11}//TA texture component gradually builds up in this phase (Fig. 7b$_1$-b$_4$).

4. Discussion

The aim of this work is to unravel the mechanisms of phase transformation and twinning in a model iHEA and their effects on strain hardening. We carried out interrupted *in-situ* and full *in-situ*
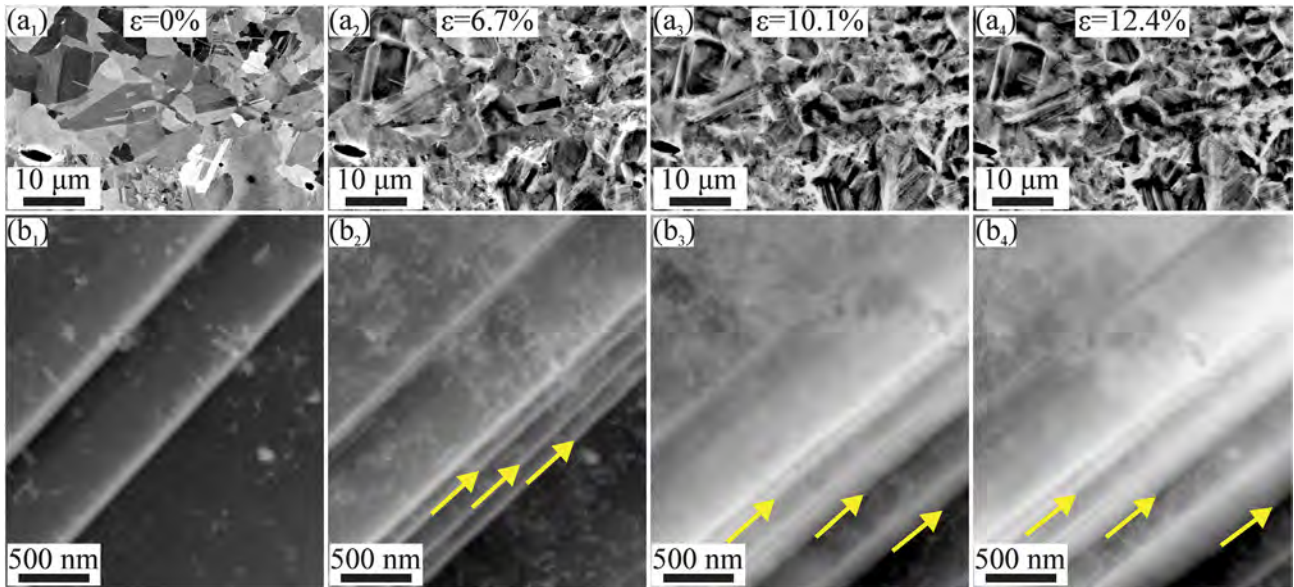
Fig. 6. *In-situ* ECCI observation of nucleation and growth of mechanical twinning. (a) Overview of the microstructure; (b) zoomed-in area showing nucleation and growth of mechanical twins. Yellow arrows in b_2-b_4 indicate the newly formed mechanical twins during *in-situ* tension. (For interpretation of the references to color in this figure legend, the reader is referred to the Web version of this article.)
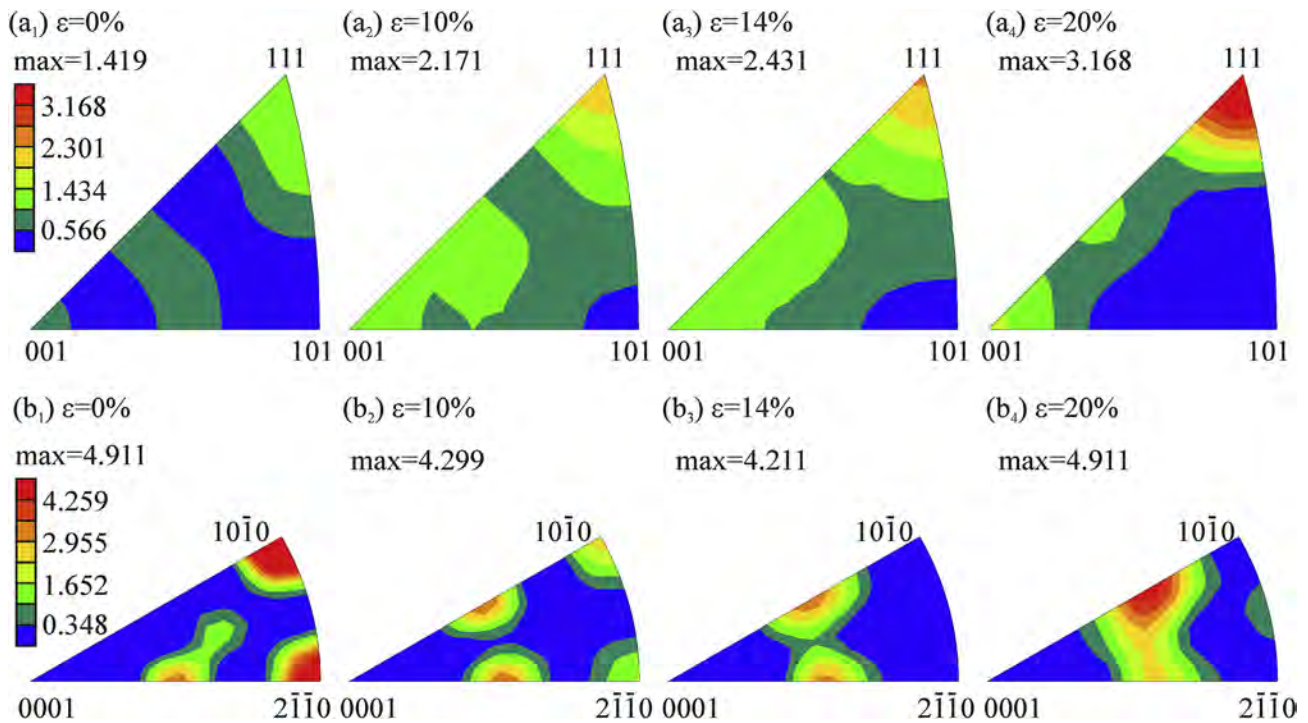

Fig. 7. Formation of crystallographic texture in (a) FCC γ phase; and (b) HCP ε phase during interrupted *in-situ* tensile testing.

tensile tests combined with EBSD/ECCI probing in the SEM for observing the evolution of dislocation/SFs patterns, deformation-driven phase transformation and mechanical twinning. A schematic sketch of microstructure evolution with straining in the iHEA is provided in Fig. 8, where black arrows point in the direction of increasing strain.

In the undeformed state, the microstructure consists of FCC γ grains and small portion of thermally-induced HCP ε phase (~0.2%) (Figs. 2b and 8a). Upon straining, the metastable FCC γ grains form

SFs along {111}//TA planes (Figs. 4, 5 and 8b). With increasing strain, multiplication and expansion of SFs inside localized microbands occur and new microbands are formed, leading to a continuous decrease in the spacing among them (Figs. 4, 5 and 8c). The dislocation and twin dominated deformation of the γ grains leads to crystallographic texture evolution and increased KAM values through the accumulation of local lattice curvature (Fig. 3). After 10%−14% strain, the overlap of SFs inside the microbanded regions reaches a critical density and marks the onset of intrinsic HCP ε
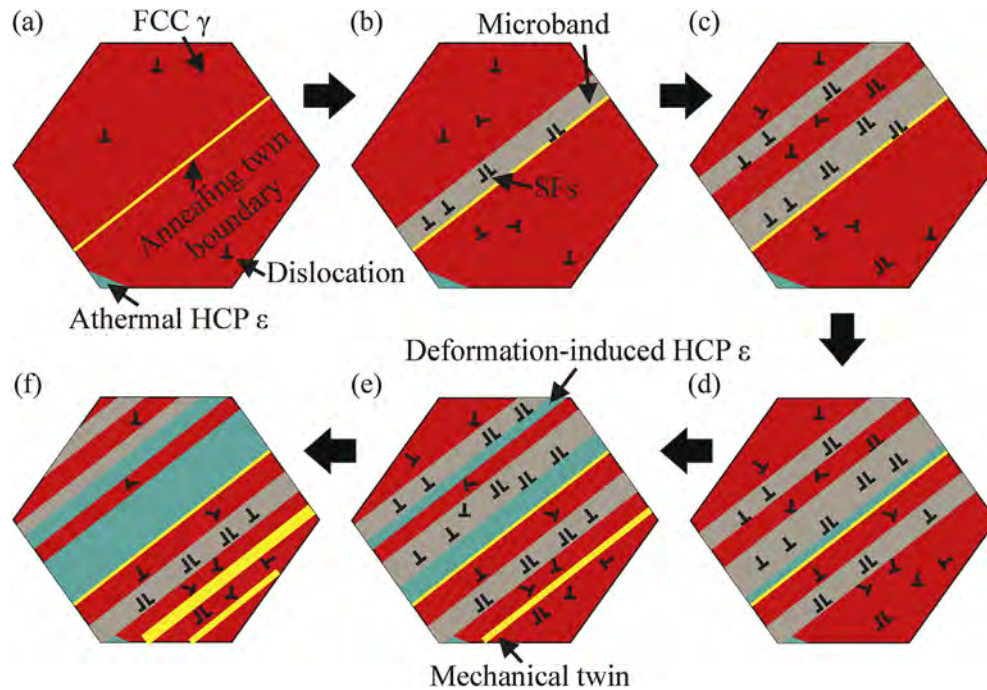
Fig. 8. Schematic sketch of microstructure evolution with straining in iHEA. Black arrows point in the direction of increasing strain values.

nucleation (Fig. 5a₃, b₃, c₂, d₂, Fig. 8d). Such critical arrangement is preferentially observed within active microbands that are adjacent to annealing twin boundaries (Figs. 5 and 8d). Instead of forming only one HCP ε nucleus within one FCC γ grain and its subsequent growth into the surrounding FCC γ matrix, many individual intrinsic ε nuclei are formed within each individual microband (Figs. 3 and 8e). With further strain, growth of deformation-induced ε into the adjacent deformed γ grains and simultaneous formation of new ε lamellae along the microbands take place (Fig. 3a₃-a₄, Fig. 8f). This sequential process of SF multiplication inside of the microbands, formation of new microbands, and the sequential transformation of these zones upon reaching a critical arrangement of SFs into ε describes the kinetics of the coupled deformation and phase transformation process in the current iHEA. After 20% strain a {111}//TA texture of the FCC γ grains has been formed (Fig. 7a). As a result of the crystallographic plane match between the {111}//TA planes of the γ matrix phase and the {10−11}//TA planes of the ε phase, a continuous built-up of a {10−11}//TA deformation texture is observed for ε (Figs. 7b and 3a₂).

A corresponding nucleation model for ε formation has been proposed by Mahajan et al. [42]. According to this approach, two perfect dislocations split into faulted pairs and react on primary slip planes. The resulting product consists of an ensemble of three Shockley partials on every second {111} plane. Each stacking fault is bounded by one sessile Shockley partial back and one mobile Shockley partial front. Within one slip band, when these three Shockley partials on every second {111} plane grow into one another, the ε phase is formed. This situation characterizes the critical arrangement of SFs required for HCP ε nucleation (Fig. 3a₃, b₃, c₂, d₂). Besides the SFs also incoherent twin boundary segments can act as nucleation sites for ε phase formation [43]. Opposite to SFs, coherent twin boundaries are not expected to favor ε phase nucleation processes due to their perfect atomic arrangement [44,45]. Although we cannot fully characterize these incoherent portions in interrupted in-situ EBSD, we assume that the annealing twin boundaries acting as ε nucleation sites shown in Fig. 5 are

most likely incoherent annealing twin boundaries. One should note that in this work only a limited number of surface-intersecting FCC γ grains were examined, yet, other microstructural features, such as grain size [7,17], chemical composition [6], temperature [6], orientation [5], adjacent phase fractions [5] could all additionally influence the role of annealing twin boundaries as nucleation sites for the HCP phase.

After nucleation, the growth of ε takes place through the motion of mobile Shockley partials on every second {111} plane. This is in accordance with the in-situ observation of multiplication of SFs along {111} planes (Figs. 4 and 5) and the thickening of deformation-induced ε lamellae with further straining (Figs. 3 and 8d–f).

The coupling of deformation and phase transformation also explains the influence of the FCC γ grain size on its mechanical stability against deformation-stimulated phase transformation (Fig. 2). As explained in the SF model of the phase transformation mechanism, nuclei of deformation-induced HCP ε are formed within microbands after achieving a critical arrangement of SFs. At the same strain level, the density of slip bands in large γ grains (Fig. 4a₄) is much higher than that in small γ grains (Fig. 4b₄). Thus, it is plausible that a sufficient overlap of SFs within the microbands, viz. a certain necessary critical arrangement of SFs required for ε formation, is achieved in the small γ grains only at larger strains so that small γ grains are more stable against this type of transformation. The grain size effect on the stability of γ grains against athermal transformation has been studied before regarding its competing effects on nucleation and growth of the ε phase [17,46—48]: On the one hand, a grain boundary acts as preferential nucleation site for phase transformation. Thus, the Mahajan nucleation model suggests that earlier nucleation is favored in γ grains with smaller size due to their higher ratio of grain boundary area to volume [47]. On the other hand, grain boundaries stabilize γ grains against athermal phase transformation by hindering the growth of the ε plates [48]. Also, dislocation pile-ups in front of grain boundaries result in strain field that produce back stress impeding dislocation motion. Due to decreased resistance to plastic

deformation in large γ grains, they deform more and accumulate more localized strain by formation of microbands with higher density of SFs (Fig. 4). Eventually, a critical arrangement of SFs sufficient for ε phase nucleation within microbands is achieved easier in large γ grains (Fig. 4). Thus, large γ grains have lower mechanical stability against deformation-induced phase transformation than small γ grains (Fig. 2).

Besides phase transformation, mechanical twinning is also active during the deformation process. At a local engineering strain of 6.7%, which corresponds to a global engineering stress of ~736 MPa, thin mechanical twin lamellae have been formed in γ grains with a size of ~10 μm. However, since we used a relatively small tensile sample for the *in-situ* ECCI probing, compared to the macroscopic tensile testing, the influence of sample dimension and geometry on the results should also be considered [49,50]. Thickness and gauge length of tensile samples can influence the necking geometry, fracture modes and strain distribution [50]. In the current iHEA specimen, for the same local strain of 6.7%, the corresponding engineering stress obtained from the *in-situ* ECCI SEM test exceeds that of the macroscopic tensile test by ~57 MPa (Figs. 1f and 4). In addition, mechanical twinning was activated during continuous loading and ECCI observations were carried out afterwards, e.g. at a stress level above the twinning stress. Thus, 736 MPa should be treated as upper bound of the twinning stress in the γ grains with a size of ~10 μm in the current iHEA [51]. Laplanche et al. reported a twinning stress in an equiatomic C-free CrMnFeCoNi HEA at room temperature of 720 ± 30 MPa [13,51]. The twin nucleation stress increases with decreasing grain size [52,53], e.g. following essentially the stress dependence of the Hall-Petch relationship [54–56]. Since the majority of the γ grains in the current alloy has a grain size below 7.9 μm (Fig. 2a), a higher stress is required to activate twinning in these grains. Hence, mechanical twinning becomes more prevalent as a strain hardening mechanism at stress levels higher than 736 MPa. At larger strains (10.1% and 12.4%) we observe that the twins grow preferentially in one direction, such as for instance highlighted by the yellow arrows in Fig. 6. This finding matches the prediction of the twinning model proposed by Mahajan et al. [57]: The formation of ε and mechanical twinning are crystallographically related mechanisms. While twins in FCC γ form through the passage of Shockley partial dislocations on every {111} plane, HCP ε forms in an FCC γ host crystal through the passage of partials on every second {111} plane [42,57–60]. On individual {111} planes, each SF is bounded by one sessile Shockley partial dislocation and one mobile Shockley partial dislocation. Only when exposed to a corresponding stress and under favorable energy conditions, the mobile partial dislocations move resulting in twin growth (Figs. 6 and 8e–f).

In summary, in this study we showed that the Fe-30Mn-10Co-10Cr-0.5C (at. %) iHEA deforms by a complex hierarchy of interconnected mechanisms: At low and intermediate strains deformation is dominated by dislocation and partial dislocation slip. Topologically this slip activity is not homogeneous but localizes into confined narrow microbands of ~50 nm width (Figs. 4 and 5). These microbands are crystallographically {111} aligned zones of concentrated {111} slip inside the FCC γ matrix. Upon reaching a critical arrangement of SFs in these microbands, they start to gradually transform along these bands into HCP ε. These various mechanisms and their sequence of activation were also observed to depend on grain size: Smaller γ grains have been directly observed by *in-situ* EBSD to resist with higher mechanical stability against the deformation-driven athermal phase transformation into ε. Mechanical twinning is also activated in the microbands. The upper bound for the twinning stress in γ grains with an average size of ~10 μm in the current iHEA is 736 MPa. Therefore, twinning in the majority of the γ grains with a size below 7.9 μm is activated

preferentially at higher stress levels, e.g. the contribution of twinning to strain hardening is more pronounced at high loads. Thus, for further alloy tuning it is an option to optimize the grain size distribution along these lines for individually adjusting the activation of dislocation-mediated plasticity, phase transformation and mechanical twinning at the different deformation stages to match a desired stress-strain and strain hardening profile.

5. Conclusions

We studied the mechanisms of deformation, phase transformation and mechanical twinning in a Fe-30Mn-10Co-10Cr-0.5C (at. %) iHEA alloy using interrupted *in-situ* and *in-situ* EBSD and ECCI probing during tensile testing in the SEM. The main conclusions are:

(1) Deformation takes place by formation of SFs and dislocations, deformation-driven phase transformation from FCC γ into HCP ε and by mechanical twinning.

(2) Upon straining, parallel arrangements of SFs along {111} planes form within the γ grains. With increasing strain, microbands are continuously formed and their spacing gradually decreases.

(3) When reaching a sufficient frequency in overlapping SFs, nuclei of HCP ε phase are formed within the microbands. Incoherent annealing twin boundaries in the γ grains are preferential nucleation sites for ε transformation in the current iHEA. With further deformation, the HCP ε phase grows into the neighboring deformed FCC γ matrix.

(4) Smaller γ grain size increases mechanical stability against deformation-induced athermal phase transformation.

(5) The upper bound for the macroscopic polycrystal twinning stress is ~736 MPa for γ grains with a size of ~10 μm at room temperature. With increasing deformation, new twin lamellae are continuously nucleated. Growth of twins proceeds in one preferred direction.

(6) During deformation, a {111}//TA texture is formed for the FCC γ phase and a {10–11}//TA texture for the deformation-induced HCP ε phase.

Acknowledgements

References

[1] B. Cantor, I.T.H. Chang, P. Knight, A.J.B. Vincent, Microstructural development in equiatomic multicomponent alloys, Mater. Sci. Eng. A 375–377 (2004) 213–218, https://doi.org/10.1016/j.msea.2003.10.257.

[2] J.W. Yeh, S.K. Chen, S.J. Lin, J.Y. Gan, T.S. Chin, T.T. Shun, et al., Nanostructured high-entropy alloys with multiple principal elements: novel alloy design concepts and outcomes, Adv. Eng. Mater. 6 (2004), https://doi.org/10.1002/adem.200300567, 299–303+274.

[3] Y. Zhang, T.T. Zuo, Z. Tang, M.C. Gao, K.A. Dahmen, P.K. Liaw, et al., Microstructures and properties of high-entropy alloys, Prog. Mater. Sci. 61 (2014) 1–93, https://doi.org/10.1016/j.pmatsci.2013.10.001.

[4] Z. Li, K.G. Pradeep, Y. Deng, D. Raabe, C.C. Tasan, Metastable high-entropy dual-phase alloys overcome the strength–ductility trade-off, Nature 534 (2016) 227–230, https://doi.org/10.1038/nature17981.

[5] L. Ma, L. Wang, Z. Nie, F. Wang, Y. Xue, J. Zhou, et al., Reversible deformation-induced martensitic transformation in Al0.6CoCrFeNi high-entropy alloy investigated by in situ synchrotron-based high-energy X-ray diffraction, Acta Mater. 128 (2017) 12–21, https://doi.org/10.1016/j.actamat.2017.02.014.

[6] J. Moon, Y. Qi, E. Tabachnikova, Y. Estrin, W.M. Choi, S.H. Joo, et al., Deformation-induced phase transformation of Co20Cr26Fe20Mn20Ni14 high-entropy alloy during high-pressure torsion at 77 K, Mater. Lett. 202 (2017) 86–88, https://doi.org/10.1016/j.matlet.2017.05.065.

[7] Q. Tang, Y. Huang, H. Cheng, X. Liao, T.G. Langdon, P. Dai, The effect of grain

size on the annealing-induced phase transformation in an Al0·3CoCrFeNi high entropy alloy, Mater. Des. 105 (2016) 381–385, https://doi.org/10.1016/j.matdes.2016.05.079.

[8] J. Liu, C. Chen, Y. Xu, S. Wu, G. Wang, H. Wang, et al., Deformation twinning behaviors of the low stacking fault energy high-entropy alloy: an *in-situ* TEM study, Scr. Mater 137 (2017) 9–12, https://doi.org/10.1016/j.scriptamat.2017.05.001.

[9] B. Cai, B. Liu, S. Kabra, Y. Wang, K. Yan, P.D. Lee, et al., Deformation mechanisms of Mo alloyed FeCoCrNi high entropy alloy: in situ neutron diffraction, Acta Mater. 127 (2017) 471–480, https://doi.org/10.1016/j.actamat.2017.01.034.

[10] Y.L. Zhao, T. Yang, Y. Tong, J. Wang, J.H. Luan, Z.B. Jiao, et al., Heterogeneous precipitation behavior and stacking-fault-mediated deformation in a CoCrNi-based medium-entropy alloy, Acta Mater. 138 (2017) 72–82, https://doi.org/10.1016/j.actamat.2017.07.029.

[11] W. Abuzaid, H. Sehitoglu, Critical resolved shear stress for slip and twin nucleation in single crystalline FeNiCoCrMn high entropy alloy, Mater. Char. 129 (2017) 288–299, https://doi.org/10.1016/j.matchar.2017.05.014.

[12] Z. Wu, C.M. Parish, H. Bei, Nano-twin mediated plasticity in carbon-containing FeNiCoCrMn high entropy alloys, J. Alloy. Comp. 647 (2015) 815–822, https://doi.org/10.1016/j.jallcom.2015.05.224.

[13] Y.H. Jo, S. Jung, W.M. Choi, S.S. Sohn, H.S. Kim, B.J. Lee, et al., Cryogenic strength improvement by utilizing room-temperature deformation twinning in a partially recrystallized VCrMnFeCoNi high-entropy alloy, Nat. Commun. 8 (2017) 15719, https://doi.org/10.1038/ncomms15719.

[14] S.W. Wu, G. Wang, J. Yi, Y.D. Jia, I. Hussain, Q.J. Zhai, et al., Strong grain-size effect on deformation twinning of an Al0.1CoCrFeNi high-entropy alloy, Mater. Res. Lett. 5 (2017) 276–283, https://doi.org/10.1080/21663831.2016.1257514.

[15] S.H. Joo, H. Kato, M.J. Jang, J. Moon, C.W. Tsai, J.W. Yeh, et al., Tensile deformation behavior and deformation twinning of an equimolar CoCrFeMnNi high-entropy alloy, Mater. Sci. Eng. A 689 (2017) 122–133, https://doi.org/10.1016/j.msea.2017.02.043.

[16] Z. Li, C.C. Tasan, H. Springer, B. Gault, D. Raabe, Interstitial atoms enable joint twinning and transformation induced plasticity in strong and ductile high-entropy alloys, Sci. Rep. 7 (2017) 40704, https://doi.org/10.1038/srep40704.

[17] Z. Li, C.C. Tasan, K.G. Pradeep, D. Raabe, A TRIP-assisted dual-phase high-entropy alloy: grain size and phase fraction effects on deformation behavior, Acta Mater. 131 (2017) 323–335, https://doi.org/10.1016/j.actamat.2017.03.069.

[18] Z. Li, D. Raabe, Strong and ductile non-equiatomic high-entropy alloys: design, processing, microstructure, and mechanical properties, Jom 69 (2017) 2099–2106, https://doi.org/10.1007/s11837-017-2540-2.

[19] D.T. Pierce, J.A. Jiménez, J. Bentley, D. Raabe, J.E. Wittig, The influence of stacking fault energy on the microstructural and strain-hardening evolution of Fe−Mn−Al−Si steels during tensile deformation, Acta Mater. 100 (2015) 178–190, https://doi.org/10.1016/j.actamat.2015.08.030.

[20] B. Mahato, S.K. Shee, T. Sahu, S.G. Chowdhury, P. Sahu, D.A. Porter, An effective stacking fault energy viewpoint on the formation of extended defects and their contribution to strain hardening in a Fe − Mn − Si − Al twinning-induced plasticity steel, Acta Mater. 86 (2015) 69–79, https://doi.org/10.1016/j.actamat.2014.12.015.

[21] T.-H. Lee, E. Shin, C.-S. Oh, H.-Y. Ha, S.-J. Kim, Correlation between stacking fault energy and deformation microstructure in high-interstitial-alloyed austenitic steels, Acta Mater. 58 (2010) 3173–3186, https://doi.org/10.1016/j.actamat.2010.01.056.

[22] I. Gutierrez-Urrutia, D. Raabe, Multistage strain hardening through dislocation substructure and twinning in a high strength and ductile weight-reduced Fe−Mn−Al−C steel, Acta Mater. 60 (2012) 5791–5802, https://doi.org/10.1016/j.actamat.2012.07.018.

[23] D. Yan, C.C. Tasan, D. Raabe, High resolution in situ mapping of microstrain and microstructure evolution reveals damage resistance criteria in dual phase steels, Acta Mater. 96 (2015) 399–409, https://doi.org/10.1016/j.actamat.2015.05.038.

[24] C.C. Tasan, J.P.M. Hoefnagels, M.G.D. Geers, Microstructural banding effects clarified through micrographic digital image correlation, Scr. Mater 62 (2010) 835–838, https://doi.org/10.1016/j.scriptamat.2010.02.014.

[25] M.-M. Wang, C.C. Tasan, D. Ponge, A. Kostka, D. Raabe, Smaller is less stable: size effects on twinning vs. transformation of reverted austenite in TRIP-maraging steels, Acta Mater. 79 (2014) 268–281, https://doi.org/10.1016/j.actamat.2014.07.020.

[26] G.K. Tirumalasetty, M.A. van Huis, C. Kwakernaak, J. Sietsma, W.G. Sloof, H.W. Zandbergen, Deformation-induced austenite grain rotation and transformation in TRIP-assisted steel, Acta Mater. 60 (2012) 1311–1321, https://doi.org/10.1016/j.actamat.2011.11.026.

[27] S. Zaefferer, A critical review of orientation microscopy in SEM and TEM, Cryst. Res. Technol. 46 (2011) 607–628, https://doi.org/10.1002/crat.201100125.

[28] M.-M. Wang, C.C. Tasan, D. Ponge, A.-C. Dippel, D. Raabe, Nanolaminate transformation-induced plasticity–twinning-induced plasticity steel with dynamic strain partitioning and enhanced damage resistance, Acta Mater. 85 (2015) 216–228, https://doi.org/10.1016/j.actamat.2014.11.010.

[29] D. De Knijf, C. Föjer, L.A.I. Kestens, R. Petrov, Factors influencing the austenite stability during tensile testing of Quenching and Partitioning steel determined via *in-situ* Electron Backscatter Diffraction, Mater. Sci. Eng. A 638 (2015)

[30] W.S. Li, H.Y. Gao, H. Nakashima, S. Hata, W.H. Tian, *In-situ* study of the deformation-induced rotation and transformation of retained austenite in a low-carbon steel treated by the quenching and partitioning process, Mater. Sci. Eng. A 649 (2016) 417–425, https://doi.org/10.1016/j.msea.2015.09.076.

[31] Y.B. Das, A.N. Forsey, T.H. Simm, K.M. Perkins, M.E. Fitzpatrick, S. Gungor, et al., In situ observation of strain and phase transformation in plastically deformed 301 austenitic stainless steel, Mater. Des. 112 (2016) 107–116, https://doi.org/10.1016/j.matdes.2016.09.057.

[32] A.A. Saleh, E.V. Pereloma, A.A. Gazder, Microstructure and texture evolution in a twinning-induced-plasticity steel during uniaxial tension, Acta Mater. 61 (2013) 2671–2691, https://doi.org/10.1016/j.actamat.2013.01.051.

[33] S. Zaefferer, N.-N. Elhami, Theory and application of electron channelling contrast imaging under controlled diffraction conditions, Acta Mater. 75 (2014) 20–50, https://doi.org/10.1016/j.actamat.2014.04.018.

[34] M. Wang, C. Tasan, D. Ponge, D. Raabe, Spectral TRIP enables ductile 1.1GPa martensite, Acta Mater. 111 (2016) 262–272, https://doi.org/10.1016/j.actamat.2016.03.070.

[35] I. Gutierrez-Urrutia, S. Zaefferer, D. Raabe, Coupling of electron channeling with EBSD: toward the quantitative characterization of deformation structures in the SEM, Jom 65 (2013) 1229–1236, https://doi.org/10.1007/s11837-013-0678-0.

[36] I. Gutierrez-Urrutia, S. Zaefferer, D. Raabe, Electron channeling contrast imaging of twins and dislocations in twinning-induced plasticity steels under controlled diffraction conditions in a scanning electron microscope, Scr. Mater 61 (2009) 737–740, https://doi.org/10.1016/j.scriptamat.2009.06.018.

[37] M. Koyama, E. Akiyama, K. Tsuzaki, D. Raabe, Hydrogen-assisted failure in a twinning-induced plasticity steel studied under in situ hydrogen charging by electron channeling contrast imaging, Acta Mater. 61 (2013) 4607–4618, https://doi.org/10.1016/j.actamat.2013.04.030.

[38] M. Calcagnotto, D. Ponge, E. Demir, D. Raabe, Orientation gradients and geometrically necessary dislocations in ultrafine grained dual-phase steels studied by 2D and 3D EBSD, Mater. Sci. Eng. A 527 (2010) 2738–2746, https://doi.org/10.1016/j.msea.2010.01.004.

[39] C.C. Tasan, J.P.M. Hoefnagels, M. Diehl, D. Yan, F. Roters, D. Raabe, Strain localization and damage in dual phase steels investigated by coupled *in-situ* deformation experiments and crystal plasticity simulations, Int. J. Plast. 63 (2014) 198–210, https://doi.org/10.1016/j.ijplas.2014.06.004.

[40] E. Demir, D. Raabe, N. Zaafarani, S. Zaefferer, Investigation of the indentation size effect through the measurement of the geometrically necessary dislocations beneath small indents of different depths using EBSD tomography, Acta Mater. 57 (2009) 559–569, https://doi.org/10.1016/j.actamat.2008.09.039.

[41] J.D. Yoo, K.T. Park, Microband-induced plasticity in a high Mn-Al-C light steel, Mater. Sci. Eng. A 496 (2008) 417–424, https://doi.org/10.1016/j.msea.2008.05.042.

[42] S. Mahajan, M. Green, D. Brasen, A model for the FCC→ HCP transformation, its applications, and experimental evidence, Metall. Trans. A 8 (1977) 283–293, https://doi.org/10.1007/BF02661642.

[43] G.B. Olson, M. Cohen, A general mechanism of martensitic nucleation: Part II. FCC-BCC and other martensitic transformations, Metall. Trans. A 7A (1976) 1905–1914.

[44] J.A. Brown, N.M. Ghoniem, Structure and motion of junctions between coherent and incoherent twin boundaries in copper, Acta Mater. 57 (2009) 4454–4462, https://doi.org/10.1016/j.actamat.2009.06.009.

[45] L. Liu, J. Wang, S.K. Gong, S.X. Mao, Atomistic observation of a crack tip approaching coherent twin boundaries, Sci. Rep. 4 (2014) 3–6, https://doi.org/10.1038/srep04397.

[46] S. Takaki, H. Nakatsu, Y. Tokunaga, Effects of austenite grain size on ε martensitic transformation in Fe-15mass%Mn alloy, Mater. Trans. 34 (1993) 489–495, https://doi.org/10.2320/matertrans1989.34.489.

[47] J.R.C. Guimarães, P.R. Rios, Martensite start temperature and the austenite grain-size, J. Mater. Sci. 45 (2010) 1074–1077, https://doi.org/10.1007/s10853-009-4044-0.

[48] W.C. Leslie, R.L. Miller, The stabilization of austenite by closely spaced boundaries, ASM Trans. Q 57 (1964) 972–979.

[49] A.V. Sergueeva, J. Zhou, B.E. Meacham, D.J. Branagan, Gage length and sample size effect on measured properties during tensile testing, Mater. Sci. Eng. A 526 (2009) 79–83, https://doi.org/10.1016/j.msea.2009.07.046.

[50] Y.H. Zhao, Y.Z. Guo, Q. Wei, A.M. Dangelewicz, C. Xu, Y.T. Zhu, et al., Influence of specimen dimensions on the tensile behavior of ultrafine-grained Cu, Scr. Mater 59 (2008) 627–630, https://doi.org/10.1016/j.scriptamat.2008.05.031.

[51] G. Laplanche, A. Kostka, O.M. Horst, G. Eggeler, E.P. George, Microstructure evolution and critical stress for twinning in the CrMnFeCoNi high-entropy alloy, Acta Mater. 118 (2016) 152–163, https://doi.org/10.1016/j.actamat.2016.07.038.

[52] D.R. Steinmetz, T. Jäpel, B. Wietbrock, P. Eisenlohr, I. Gutierrez-Urrutia, A. Saeed–Akbari, et al., Revealing the strain-hardening behavior of twinning-induced plasticity steels: theory, simulations, experiments, Acta Mater. 61 (2013) 494–510, https://doi.org/10.1016/j.actamat.2012.09.064.

[53] S.L. Wong, M. Madivala, U. Prahl, F. Roters, D. Raabe, A crystal plasticity model for twinning- and transformation-induced plasticity, Acta Mater. 118 (2016) 140–151, https://doi.org/10.1016/j.actamat.2016.07.032.

[54] I. Gutierrez-Urrutia, S. Zaefferer, D. Raabe, The effect of grain size and grain orientation on deformation twinning in a Fe−22wt.% Mn−0.6wt.% C TWIP steel, Mater. Sci. Eng. A 527 (2010) 3552–3560, https://doi.org/10.1016/

j.msea.2010.02.041.

[55] W.L. Wang, X.L. Wang, W. Mei, J. Sun, Role of grain size in tensile behavior in twinning-induced plasticity β Ti-20V-2Nb-2Zr alloy, Mater. Char. 120 (2016) 263—267, https://doi.org/10.1016/j.matchar.2016.09.016.

[56] K.M. Rahman, V.A. Vorontsov, D. Dye, The effect of grain size on the twin initiation stress in a TWIP steel, Acta Mater. 89 (2015) 247—257, https://doi.org/10.1016/j.actamat.2015.02.008.

[57] S. Mahajan, G. Chin, Formation of deformation twins in fcc crystals, Acta Metall. 21 (1973) 1353.

[58] G.B. Olson, M. Cohen, A mechanism for the strain-induced nucleation of martensitic transformations, J. Less-Common Met. 28 (1972) 107—118.

[59] J.W. Christian, S. Mahajan, Deformation twinning, Prog. Mater. Sci. 39 (1995) 1—157, https://doi.org/10.1016/0079-6425(94)00007-7.

[60] J.W. Christian, A theory of the transformation in pure cobalt, Proc. R. Soc. London Ser. A. Math. Phys. Sci. 206 (1951), 51 LP-64, http://rspa.royalsocietypublishing.org/content/206/1084/51.abstract.